Cell Reports
Physical Science

CellPress
OPEN ACCESS

Article

Integrated wearable smart sensor system for real-time multi-parameter respiration health monitoring

Li et al. propose a respiratory monitoring sensor (RMS) system for artificial intelligence (AI)-assisted diagnosis of respiration by detection of multi-self-calibrated parameters. This system has the potential advantages of home health monitoring, smart early-stage medical diagnosis, and auxiliary telemedicine.

Yingzhe Li, Chaoran Liu, Haiyang Zou, ..., Xucong Wang, Gaofeng Wang, Zhong Lin Wang

liucr@hdu.edu.cn (C.L.)
donglinxi@hdu.edu.cn (L.D.)
libozhao@mail.xjtu.edu.cn (L.Z.)
zhong.wang@mse.gatech.edu (Z.L.W.)

Highlights

A conceptual, logical, and physical model of respiratory monitoring

Respiration parameters self-calibration with an accuracy >95.21%

Multi-physiological parameters for auxiliary diagnosing diseases

Li et al., Cell Reports Physical Science 4, 101191
January 18, 2023
https://doi.org/10.1016/j.xcrp.2022.101191

Cell Reports
Physical Science

CellPress
OPEN ACCESS

Article

Integrated wearable smart sensor system for real-time multi-parameter respiration health monitoring

Yingzhe Li,[1,8] Chaoran Liu,[1,2,8,9,*] Haiyang Zou,[2,7,8] Lufeng Che,[3] Peng Sun,[1] Jiaming Yan,[1] Wenzhu Liu,[4] Zhenlong Xu,[1] Weihuang Yang,[1] Linxi Dong,[1,*] Libo Zhao,[5,*] Xucong Wang,[1] Gaofeng Wang,[1] and Zhong Lin Wang[2,6,*]

SUMMARY

Monitoring respiration is vital for personal diagnosis of chronic diseases. However, the existing respiratory sensors have severe limitations, such as single function, finite detection parameters, and lack of smart signal analysis. Here, we present an integrated wearable and low-cost smart respiratory monitoring sensor (RMS) system with artificial intelligence (AI)-assisted diagnosis of respiratory abnormality by detecting multi-parameters of human respiration. Coupling with intelligent analysis and data mining algorithms embedded in a phone app, the lighter system of 7.3 g can acquire real-time self-calibrated parameters, including breathing frequency, apnea hypopnea index (AHI), vital capacity (VC), peak expiratory flow (PEF), and other respiratory indexes with an accuracy >95.21%. The data can be wirelessly transferred to the user's data cloud terminal. The RMS system enables comprehensive multi-physiological parameters analysis for auxiliary diagnosing and classifying diseases, including sleep apnea, rhinitis, and chronic lung diseases, as well as rehabilitation of COVID-19, and exhibits advantages of portable healthcare.

INTRODUCTION

Recently, respiratory diseases (sleep apnea, rhinitis, expiratory dyspnea, etc.) are steadily increasing due to air pollution, aging society, and unhealthy living habits. Real-time monitoring of human respiration is essential for the prevention, early diagnosis, treatment, and rehabilitation of respiratory diseases. Today's existing commercial monitoring instruments in hospitals or laboratories have deficiencies of the complicated operation, bulky size, and high cost, which are inconvenient for routine real-time monitoring at home.[1,2] Especially, the coronavirus disease 2019 (COVID-19) pandemic urgently requires a portable respiratory monitor system for smart tracking of the survivor's health status.

The self-powered respiratory monitor sensor enabled by triboelectric nanogenerator (TENG) has attracted broad attention due to its high sensitivity, portability, and flexibility.[3,4] Extensive research focused on sensor materials,[5–8] structures,[9–13] and manufacturing processes[14,15] to enhance the sensitivity, human suitability, and wearability.[16,17] Nevertheless, the current respiratory sensor based on TENG has still many deficiencies, such as limited detection parameters of breathing, single function of detection, and poor anti-interference.[18] In addition, it still lacks an integrated smart

[1]Ministry of Education Engineering Research Center of Smart Microsensors and Microsystems, College of Electronics and Information, Hangzhou Dianzi University, Hangzhou 310018, P. R. China

[2]School of Materials Science and Engineering, Georgia Institute of Technology, Atlanta, GA 30332-0245, USA

[3]College of Information Science & Electronic Engineering, Zhejiang University, Hangzhou 310027, P. R. China

[4]Research Center for New Energy Technology, Shanghai Institute of Microsystem and Information Technology (SIMIT), Chinese Academy of Sciences (CAS), Shanghai 201800, P. R. China

[5]State Key Laboratory for Manufacturing Systems Engineering, International Joint Laboratory for Micro/Nano Manufacturing and Measurement Technologies, Collaborative Innovation Center of Suzhou Nano Science and Technology, School of Mechanical Engineering, Xi'an Jiaotong University, Xi'an 710071, China

[6]Beijing Institute of Nanoenergy and Nanosystems, Chinese Academy of Sciences, Beijing 101400, P. R. China

[7]College of Materials Science and Engineering, Sichuan University, Chengdu 610065, People's Republic of China

[8]These authors contributed equally

[9]Lead contact

*Correspondence: liucr@hdu.edu.cn (C.L.), donglinxi@hdu.edu.cn (L.D.), libozhao@mail.xjtu.edu.cn (L.Z.), zhong.wang@mse.gatech.edu (Z.L.W.)

https://doi.org/10.1016/j.xcrp.2022.101191

system with signal processing, data transmitting, data analysis, and data storage, which is significant for real-time monitoring, remote control, multi-parameter sensing, information extraction, and auxiliary medical diagnosis.[19,20]

Herein, we propose a self-powered and wearable RMS system based on TENG to interactively monitor human breath. The top triboelectric film (flutter layer) moves up and down due to the breathing air flow, which induces related electrical respiration signals. The flexible respiratory sensor achieves a sensitivity of 0.719 V/(m/s) under the airflow speed range from 0 to 7 m/s, which well fits the airflow speed of breathing. More importantly, the respiratory sensor attached under the nose can simultaneously capture various parameters of the human breathing (e.g., respiration depth, frequency, respiratory interval time, apnea hypopnea index [AHI], vital capacity [VC], and peak expiratory flow [PEF]). With the integrated system of signal processing, wireless transmission module, user terminal with data calibration and analysis, the smart system achieves the multi-functions of respiratory signal wireless transmission, real-time display, information extraction, and health status diagnosis. Particularly, the respiration signal can be accurately detected under different human breathing states and ambient factors upon the various environmental conditions (humidity of 25%–75% and temperature of 23–55°C). This work provides a long-term effective solution for monitoring human respiratory diseases and portable intelligent auxiliary telemedicine.

RESULTS

Working mechanism of RMS

Based on human respiration characteristics, we developed a self-powered flexible respiratory monitor sensor enabled by TENG (Figure 1B and Video S7), which consists of a polydimethylsiloxane (PDMS) frame, a Kapton-Al flutter layer, a Cu-polytetrafluoroethylene (PTFE) triboelectric underlying layer, and a fixed copper tube, shown as Fig. S5. The mechanism of the sensor relies on the contact-separation mode TENG.[21,22] The two triboelectric layers contact or separate driven by the respiration flow, which should meet the requirement of flutter critical velocity U_f and film intrinsic parameters, including stiffness E, length L, and triboelectric layer gap D (Equation 1 and Note S1). To drive the flutter layer, the normal human respiration flow range (1.2–9 m/s)[23] should be greater than the critical velocity. Thus, we developed a size-optimized respiratory sensor with a minimum flow rate of 0.5 m/s (Figure S1).

$$U_f \sim A_1 \sqrt{\frac{ED^3}{\rho_a L^3}} \quad \text{(Equation 1)}$$

The sensor working process has three main situations: initial state, inhale and exhale states (Figure S5C). In the initial state, the flutter layer naturally droops and slightly contacts with the underlying film of the sensor with charge transfer between two triboelectric layers.[24] Accompanying the exhaling, the flutter layer separates from the underlying layer and moves up, which leads to a potential difference between the two electrodes. Simultaneously, it generates a current flowed from the top electrode to the bottom electrode through the external load circuit.[25–28] Inversely, the flutter layer closes to and contacts the underlying layer gradually during the inhaling process, which generates a reverse current. Thus, periodic current signals generate by a continuous breathing process.

Structure design and optimum

Generally, to optimize the output performance, some vital structural parameters are systematically investigated and modulated (Figure 2), such as triboelectric area, gap

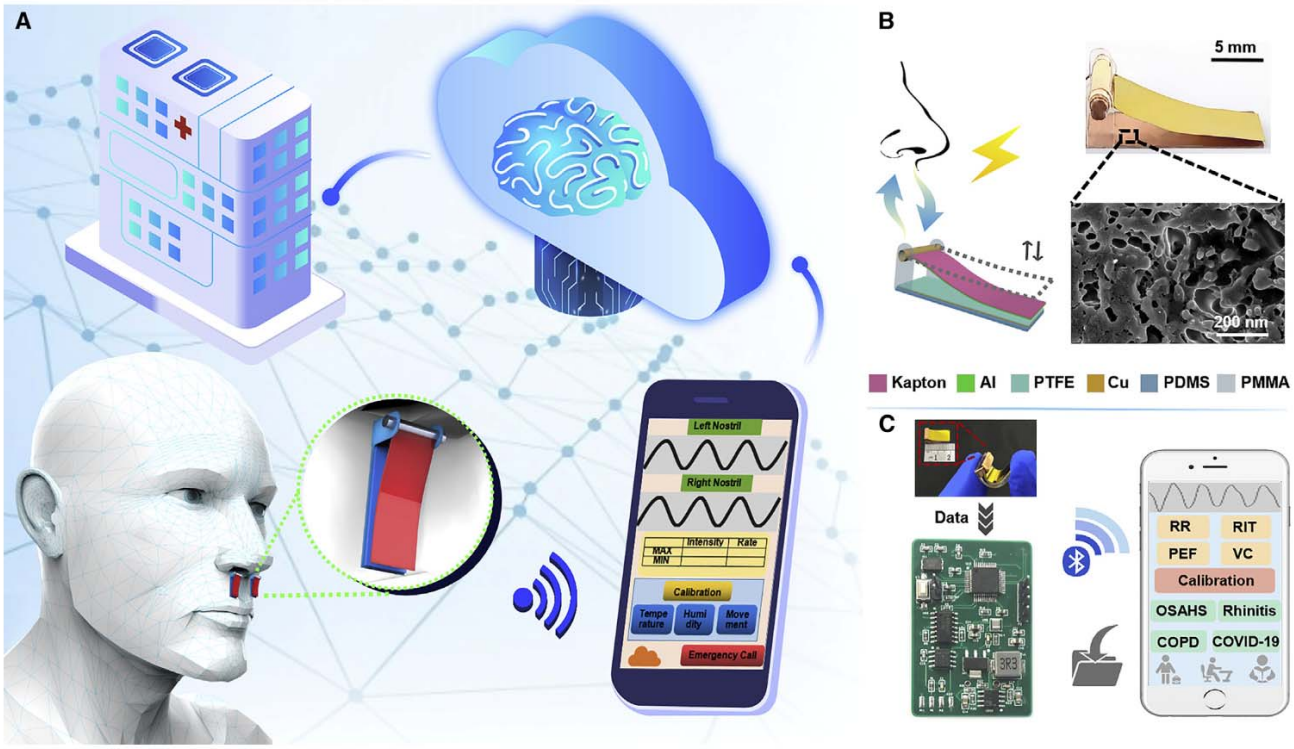

Figure 1. Structure and mechanism of the respiratory monitoring sensor system (RMSS)

(A) Schematic of multi-terminal interconnected AI respiration monitoring system.

(B) RMS working model diagram, image (scale bar, 5 mm), and scanning electron microscopy image of the PTFE surface (scale bar, 200 nm).

(C) Diagram of working process of intelligent respiratory sensing system.

height, transverse offset angle, flexible cylindrical structure, and stability of structure. Evidently, the peak output voltage rises continuously by enlarging the triboelectric area, which increases the transfer charges (Figure 2A). Also, the height of gap between top and bottom triboelectric layer is crucial for inlet flow and effective triboelectric area. A lower gap height will enlarge the triboelectric area but limit the air inlet flow due to gravity. For a higher gap height, it raises the vibration frequency of the flutter layer and lowers the triboelectric area and critical air flow speed as well (Figure S1). To obtain the optimum, we experimentally investigated the height varying from 0.4 to 1.5 cm at an average respiratory air velocity of 4.0 m/s to improve the RMS output performance. Figure 2B presents the sensor has a maximum output with the gap height of 1.2 cm due to the optimal contact area and movement under the gravity and airflow.

A rotatable supporting rod to link the flutter layer was designed, which can enhance the output performance by increasing the vibration strength (Figure 2C).[29–32] The transverse offset angle α (between human expiratory direction and attached sensor) and specific structural designs on the current output are systematically studied. Simultaneously, the output current has an enormous descent of more than 93.3% (from 133 to 7.6 nA) when the angle is set to be from 20° to 70°. While the angles vary from 0° to 20°, the output current has a lesser decline of 6.7% (from 142 to 133 nA). Therefore, the RMS has a widely transverse offset angle range from 0° to 20° to ensure the stability of output performance, which is conducive to shielding the interferential air flow (angle from 20° to 70°) from the surroundings to some extent (Figure 2D).

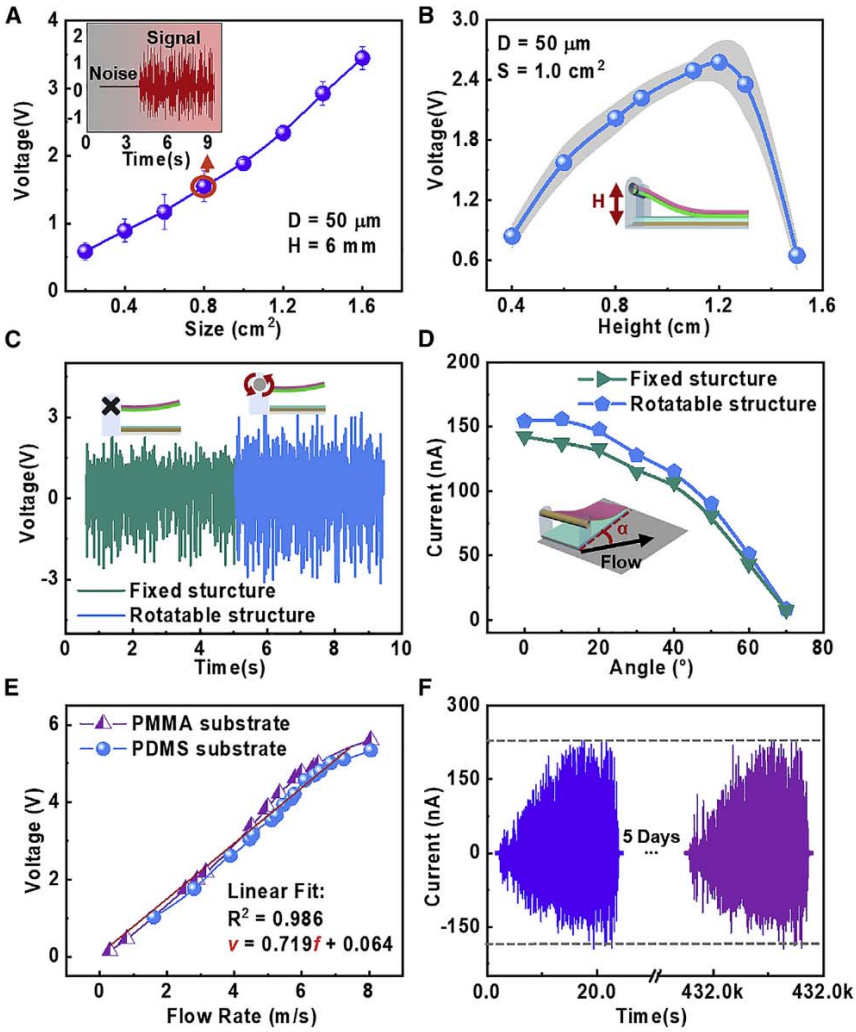

Figure 2. Basic performance and characterization with different structural parameters of RMS

(A) Voltage response of RMS (D = 50 μm, H = 6 mm) under different areas. Inset: Voltage response difference between the noise and specific air flow signal (around 2.2 m/s). Error bars indicate 1 SD.

(B) Output response (D = 50 μm, S = 1.0 cm^2) at different gap heights, and error bars show 1 SD.

(C) Voltage response of different electrode structure.

(D) Voltage output response driven by airflow in different transverse offset angle.

(E) The output voltage of RMS and voltage sensitivity fitting curve in different materials of substrate (including rigid polymethyl methacrylate [PMMA] substrate and flexible polydimethylsiloxane [PDMS] substrate).

(F) Device stability test after 5 days.

Figure 2E indicates that the measured output voltage has excellent linearity, a good load capacity, and a superior sensitivity of 0.72 V/(m/s) under the human respiration flow speed of 1.2 to 9.0 m/s.[23] Also, the as-fabricated RMS has an incisive critical velocity of 0.5 m/s (Figure S1C). A flexible substrate was applied, which can well fit human skin, thus enabling the RMS to accurately detect the exhale flow speed, frequency, and depth of respiration. Finally, working stability and long-term reliability tests were conducted to confirm the sustainability of the RMS. As shown in Figure 2F, the output current is linear, with varying the flow speed from 0 to 9 m/s. Even after 5 days, the RMS still has scarcely any attenuation of the current. We added a long-term (60 min) breathing test, as shown in Figure S10.

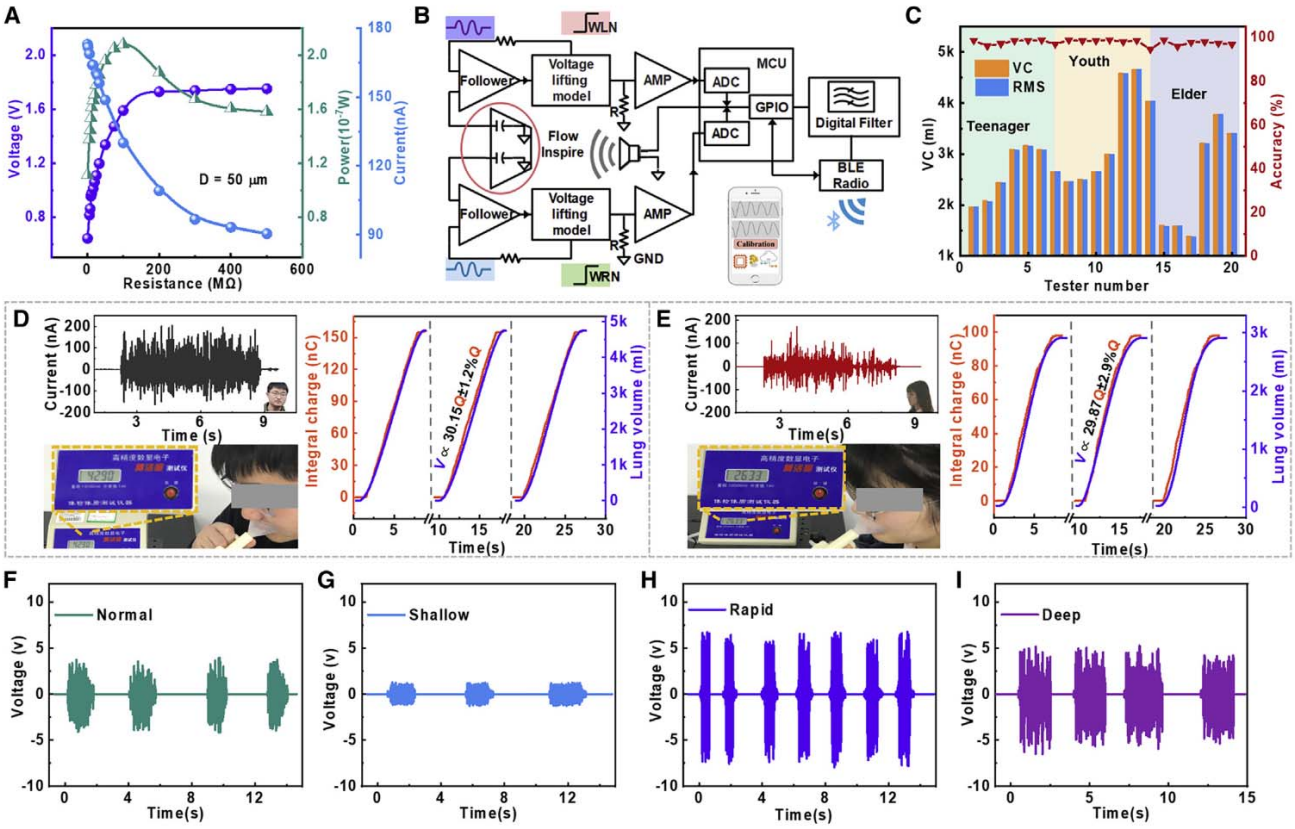

Figure 3. The wireless processing smart system of RMS and its breath test characteristics

(A) The output voltage, current, and power response of the RMS as external resistance changes.

(B) Circuit and block diagrams of the respiratory monitoring system and its wireless transmission sensor network (BLE radio). The user interface enables BLE connections to the device and activates a general-purpose input/output (GPIO) pin to obtain and transfer signals from sensor. MCU controls digital signal processing on the ADC-sampled data and wirelessly transmits the data over the BLE radio to a user interface.

(C) Bar chart and accuracy curve of *VC* values measured by commercial equipment and RMS among 20 different age and gender testers.

(D) Male and (E) female expiratory current curve tested by RMS, professional respiratory equipment test diagram, and the real-time expiratory current integral curve of RMS was compared with the real-time vital capacity test curve of professional respiratory equipment. The breathing voltage curve of (F) normal breathing, (G) shallow breathing, (H) rapid breathing, and (I) deep breathing.

Characteristics of the respiratory detection system

Signal processing circuit system is vital for RMS signal sampling, conversion, and portable display to smart monitor human respiratory symptoms. Herein, we developed a smart, tiny, real-time wireless transmission circuit system with a weight of 7.3 g and a size of 3.04 × 4.51 × 0.5 cm^3. To fit the input resistance range of analog-to-digital conversion unit (ADC), voltage follower circuits were designed to reduce the RMS impedance from the MΩ to KΩ magnitude by its feedback mechanism (Figure 3A). The voltage regulator circuit can convert RMS signal amplitude into the ADC scope. Principally, the central processing unit (CPU) performs the digital RMS signal filtering and analyzing, and then sends the data to the phone app by the Bluetooth (BLE) module (Figure 3B and Note S2). Attributing to the phone app algorithms and friendly user interface, the RMS system app achieves the artificial intelligence (AI) functions such as signal calibration, digital noise filtering, core indexes extraction, emergency alert, disease classification, and data cloud transmission (Figure S9).

The results of VC measurement on 20 volunteers mark that RMS achieved high accuracy (average accuracy >96%, containing errors generated by human operation

Table 1. Core parameters in diverse breathing states obtained from RMS

Different state	Frequency (bpm)	Time (s)	Amplitude (V)	Q_{si} (nC)	V_{se} (mL)
Normal	16	1.8	3.9	16.8	504.6
Rapid	28	1.2	6.7	20.3	610.2
Shallow	16	1.3	1.1	11.2	335.4
Deep	16	2.0	4.9	25.2	756.6

and experimental noise) in individuals of various ages and genders (Figure 3C). Prominently, we find that the expiratory volume (V_{ex}) is preferably consistent with accumulative charge (Q) by real-time integrating of the current signal, which has an approximate corresponding relation as follows:

$$V_{ex} \propto 30.0Q \pm 2.23\%Q \quad \text{(Equation 2)}$$

Thus, RMS is capable of detecting human VC based on consistency, which also has potential application for diagnosing chronic obstructive pulmonary disease (COPD) based on VC (Figures 3D, 3E, S3, and S4). Moreover, current-assisted voltage analysis of RMS is essential for respiratory parameter extraction, signal calibration, and disease classification. The respiratory states including normal, shallow, rapid, and deep breathing can be well distinguished by differences in respiratory frequency, amplitude, time, integral current (*Qsi*), and expiratory volume of single respiration (*Vse*), as shown in Figures 3F–3I. Particularly, current-assisted analysis can vastly improve the accuracy of the above parameters (Figure S2). As shown in Table 1, the frequency, time, and amplitude obtained by voltage analysis are similar between normal and deep breathing, and the *Vse* obtained by analysis of current becomes the key judgment element. Hence, RMS can detect multi-respiratory parameters in a single device.

Calibration mechanism of respiratory monitoring system

A calibration system for RMS is designed to prevent respiratory detecting results from the influence of ambient temperature and humidity.[33,34] We modeled regression fitting functions of ambient temperature and humidity by the K-Nearest Neighbor (KNN) algorithm based on the test data under the conditions of temperature (25.0°C–55.0°C) and relative humidity (25%–75%) (Figure S6). After machine learning training, the optimized functions acted as compensating factors to calibrate sensor signal, as shown in Figures 4A and 4B.

Through the KNN algorithm, the smart calibration unit can compensate the voltage amplitude loss due to the high humidity and temperature (by comparing the measured signals before and after calibration, Video S1), and recover the output signals to eliminate interference from other environmental factors. The monitoring signals are only dependent on human breathing behaviors. The calibration results indicated that expiratory flow speed was adjusted from 2.48 m/s to 3.03 m/s, closing to the standard anemometer result of 3.1 m/s, which improved the accuracy from 80.0% to 97.7% (Figure 4C). Compared with the commercial standard anemograph, the signals after calibration measured by the RMS system showed high repeatability and accuracy under complex circumstances (e.g., diverse humidity, temperature, exercise status) (Video S1).

To fit more complex conditions, the frequency-domain analysis showed that the normal respiratory frequency range is lower than the noise frequency (>10 Hz) under human various exercise states, as shown in Figure S1B. Thus, we developed a mechanical calibration method by introducing a low-pass filter and a notch filter to calibrate the respiration signal under various exercise states and improve the alarm threshold appropriately. Contemporary, the mechanical calibration component

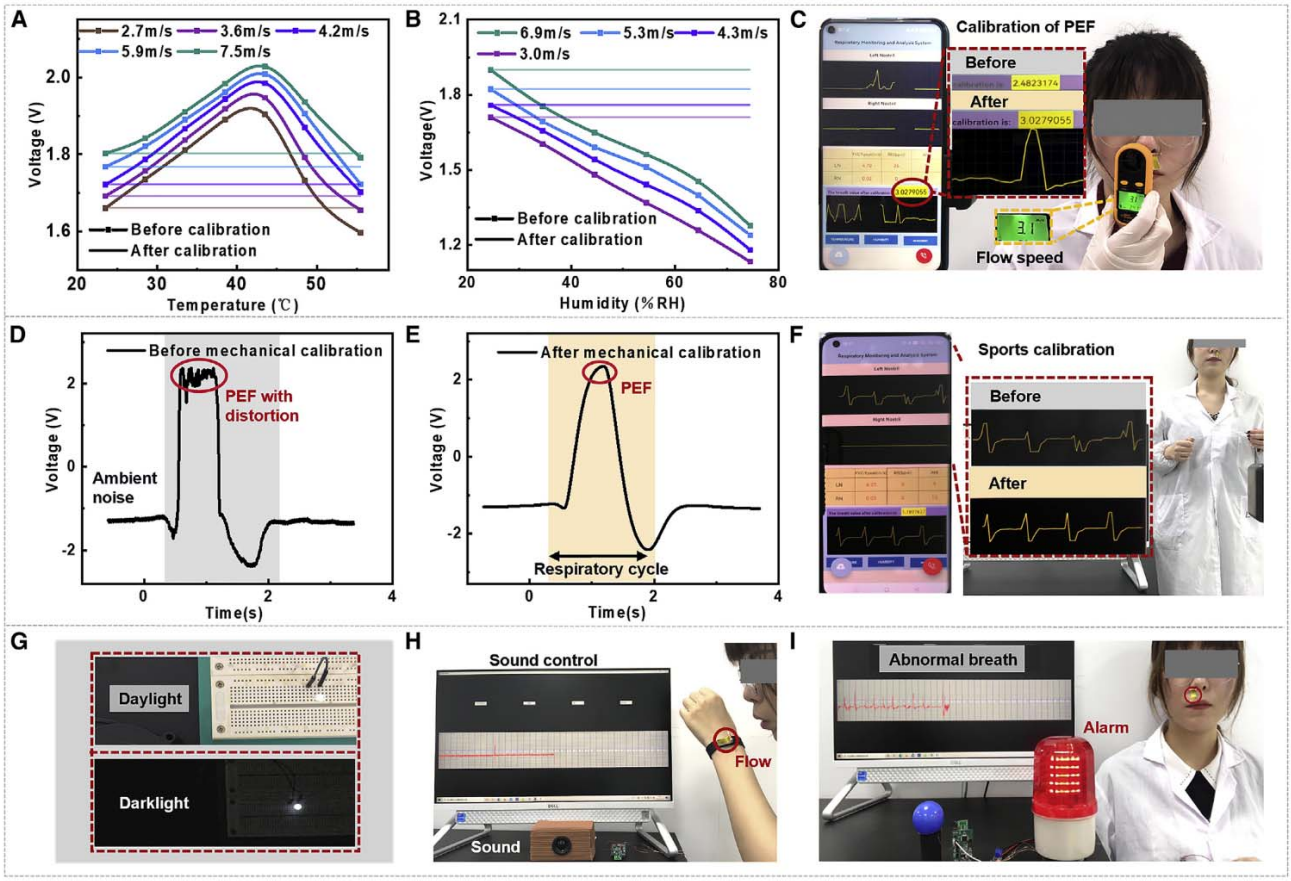

Figure 4. RMS calibration system and its basic application

(A and B)The output voltage response corresponding to different air flow velocities under different temperature (A) and (B) humidity conditions, and based on the data to calibrate temperature of the sensor.

(C) Respiratory system display before and after humidity calibration.

(D) Breath curve before mechanical calibration.

(E) Breath curve after mechanical calibration.

(F) Respiratory curve before and after mechanical calibration.

(G) RMS drives LED.

(H) Demonstration of RMS as an air flow switch to control audio equipment.

(I) Demonstration of a respiratory monitoring and abnormal alarm system.

embedded in the phone app can remarkably exclude the noise wave interference and false alarming by setting a suitable rational amplitude threshold and frequency range (Figures 4D–4F and Video S2). Therefore, the constructed calibration mechanism can overcome the obstacles of environmental change and human interference, and thereby effectively extract abnormal respiratory signals caused by diseases (Figure S12).

Based on these properties, a sensitive control system by RMS with high robustness can be set up, which enables operation of the status of sound equipment and other applications (Figure 4H and Video S3). The RMS system can monitor human abnormal breathing and trigger the alarm, as shown in Figure 4I and Video S4.

Auxiliary diseases monitor and rehabilitation

Equipped with the accurate, multi-parameter, and highly robust system, the self-powered RMS can auxiliary monitor respiratory diseases such as sleep apnea

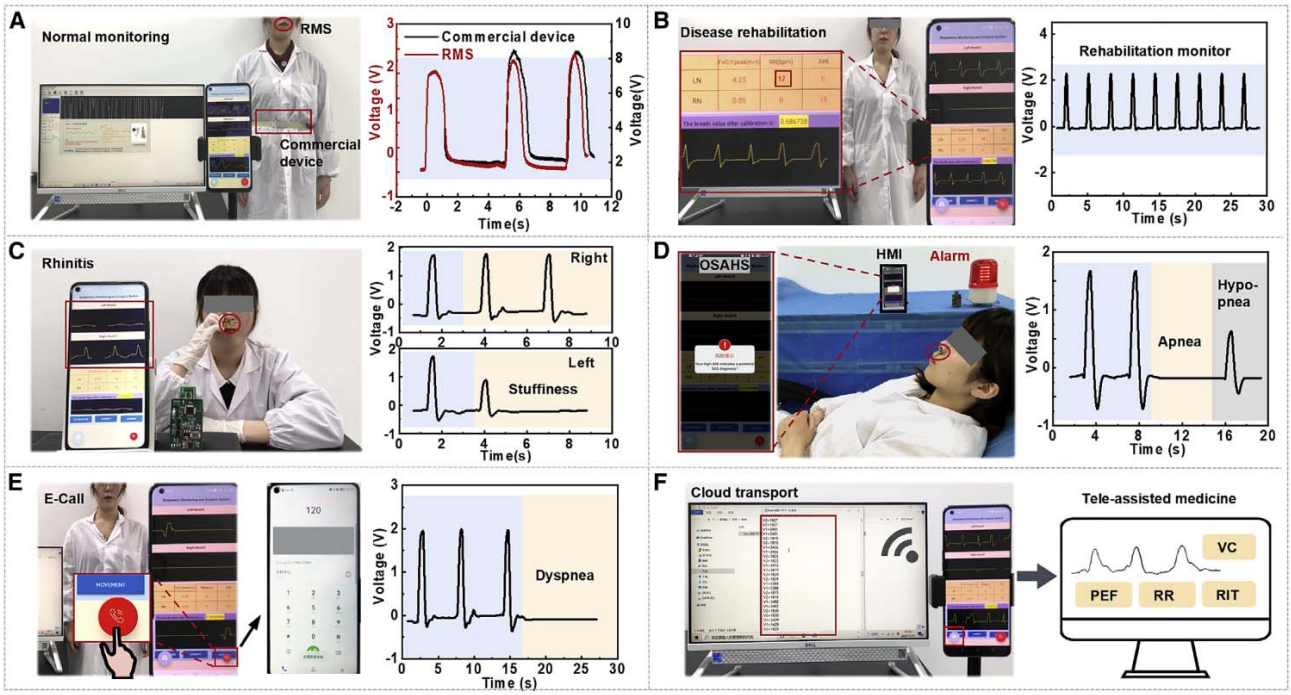

Figure 5. Applications of the RMS system for smart monitoring and adjuvant diagnosis

(A) The comparison of commercial instruments and RMS output respiratory waveform curve.

(B) Demonstration of diverse parameters in respiratory monitoring system.

(C) Respiratory monitoring system monitors simulated rhinitis symptoms in real time.

(D) The respiratory monitoring system monitors simulated symptoms of sleep apnea syndrome in real time.

(E) Emergency call function display.

(F) The respiratory monitoring system displays the signal to a remote terminal via cloud transmission.

hypopnea syndrome (OSAHS), rhinitis, asthma symptoms, and COPD through the comprehensive analysis and classification of various parameters related to their specific symptoms and breathing behaviors. Compared with commercial belt-type device, the RMS system has advantages such as reliable detection, high waveform consistency, multi-parameters, and smaller total volume (RMS system of 6.885 cm^3, commercial device of 153.0 cm^3) (Figures 5A and S7).

Given the superiority, we explored the applications of the RMS system for diagnosing and detecting abnormal breathing health status. There are symptoms such as cough, nasal obstruction, polypnea, dyspnea, and respiratory arrest for some respiratory diseases, which would cause irregular breathing behaviors. These can be monitored in real time through sensing respiration depth, frequency (RR), respiratory interval time (RIT), expiratory flow speed, and peak (PEF) (Table S1). PEF refers to the highest instantaneous expiratory flow rate, diurnal variation rate implies the change rate of PEF at different times a day, which indicates the severity of the diseases such as asthma and lung injury. Figure 5B shows detected signals from an adult respiration by the RMS system after temperature and humidity calibration, RR ~17 b/m, PEF ~4.25 m/s, RIT ~2.38 s, etc. Through the measurement under different circumstances, the PEF values of the same individual are stable after calibration. The average deviation is 3.32% through comparison with commercial equipment (tests on different days), which signifies RMS extracts these parameters fleetly and precisely (Video S1).

In addition, we explored some applications of AI-assisted disease diagnosis. COPD has an ultrahigh fatality rate of nearly 90% in low- and middle-income countries according to the latest statistics from the World Health Organization.[35] The decrement rate of vital capacity (VC) is the specificity and core index for indicating the severity of COPD.[36] Our RMS system can extract the human real-time VC by integrating the sensor current signal (i.e., transferred charges *Q*). An example is shown in Figure 3H, the final VC of a male and female are 4,748 mL (*Q* = 155.62 nC) and 2,910 mL (*Q* = 97.92 nC), respectively, with the testing precision of 98.76% and 96.78% based on the mean absolute percentage error (MAPE) method (Figure S1D). We obtained the average relative deviation of 97.77% (94.57%–98.92%) between RMS and a commercial instrument by employing 20 volunteers with diverse genders, ages, and physical states (Table S2 and Figure S4). Given the advantages of real-time data collection and analysis, wireless transmission, and low-cost, the RMS system is suitable for the primary diagnosis of COPD.

Rhinitis is a high recurrent and remediless disease with a 73% symptom of nasal congestion.[37] Subjective clinical assessments of the severity of rhinitis can be evaluated by the PEF and duration of nasal congestion symptoms.[38] A volunteer simulated the respiratory characteristics of rhinitis symptoms in the left nose. The monitoring results show the normal respiration on the right side and nasal congestion on the left nostril beginning at 4 s with a PEF descent, which demonstrates the non-interference between the right and left RMSs. Therefore, the RMS system can achieve an auxiliary diagnosis of nasal congestion diseases (Figure 5C and Video S5).

Also, OSAHS has become a common sleep disorder. The primary medical diagnosis method of polysomnography (PSG) is complex, incompatible, and high cost. The severity score of OSAHS can be divided into mild ($5 \leq$ AHI<15), moderate ($15 \leq$ AHI<30), and severe OSAH (AHI $\geq$30) based on the medical AHI ranges (/hour). The criteria of AHI increments is once a sleep apnea time (i.e., RIT) more than 10 s.[39,40] The developed phone app can extract the human AHI from the respiratory signal. Figure 5B shows the normal respiratory status with AHI = 0 during waking. In contrast, the phone app triggers an alarm when the volunteer simulated the OSAHS symptom has AHI = 12. And from the real-time breathing signals (Figure 5D), it shows that the volunteer has a respiratory apnea time of more than 6 s starting from 9 s. The hypoventilation time sustains 4 s at 15 s with the signal amplitudes descending from the average voltage of 1.8 V to 0.6 V. We also developed an alarming siren to awake the patient or neighbors if the AHI is above the normal range (Figure 5D and Video S6). These results demonstrate the feasibility and accuracy of the RMS system to monitor and detect the behaviors of OSAHS.

Noteworthily, the outbreak of COVID-19 tore across the globe due to its high infection rate. Most patients have a larger average respiratory rate and time than the normal range (12–20 bpm), even 40.3% of them accompanying dyspnea and shortness of breath.[41,42] While after recovery, there are also lung injury and some other chronic diseases (PICS), which requires long-term surveillance of patients recovered from COVID-19.[36,43,44] In a study among 100 asymptomatic cases, 60% had delayed symptoms and most of their family members had positive COVID-19 test results as well as showed signs of respiratory issues.[45,46] Hence, early detection and timely treatment are essential. With the monitoring of the RMS system, the real-time respiratory rate and time can be detected precisely. Furthermore, we developed an emergency call (E-Call) function in the phone app for patients to ask for medical

help as shown in Figure 5E (120 is a common emergency telephone number in China). And for recovery monitoring, the core indexes including VC, RR, PEF, and RIT in real time can be applied to evaluate lung health status. These parameters can be transmitted and uploaded to the specified terminal and relevant medical institutions timely by the RMS system, which is competent for COVID-19 monitoring and long-term rehabilitation surveillance (Figure 5F). We have established mathematical relationships among current (*I*), charge (*Q*), and *VC*, as well as between voltage and *PEF* (Table S3).

Given the above experiment results, the RMS system has the superiority of multiple physiological parameters detection, home health monitoring, smart early-stage medical diagnosis, and auxiliary telemedicine, which provides a novel approach for health monitoring of wireless sensor network (WSN) and the Wise Information Technology of med (WITMED) (Figure S8).

DISCUSSION

In conclusion, we have successfully developed a flexible, fast multi-parameter extracting from single detection and low-cost RMS based on TENG to accurately and smart analyze breath status. Furthermore, the relevant real-time wireless application platform is proposed for AI-assisted classification and detection of various physiological respiratory diseases.

Our highly robust RMS system can distinguish disease-induced respiratory abnormality from signal changes caused by interference based on the developed self-calibration mechanisms. The system has the potential applications even in sophisticated situations including interference from human normal activities and variation of environment temperature and humidity.

For clinical applications, the RMS platform is superior to the existing respiratory sensors in multi-parameter extraction, comprehensively evaluating physical conditions and high diagnostic accuracy. Especially, our approach provides accurate PEF and VC due to structural advantage, which could aid in AI recognition and therapy of various chronic respiratory diseases such as OSAHS, COPD, rhinitis, and the rehabilitation of COVID-19. At the same time, the device is configured to intelligent multi-terminal alarm and activates an emergency call system to avoid the risks of acute disease. Additional potential lies in the sustaining cloud transmission to boost telemedicine and prevent the spread of disease. Superior compatibility and multi-functionality enable the RMS system to combine with other facilities to provide an integrated human physiological health monitoring platform for accurate auxiliary diagnosis of diverse diseases.

EXPERIMENTAL PROCEDURES

Resource availability

Lead contact

Further information and requests for resources should be directed to and will be fulfilled by the lead contact, Chaoran Liu (liucr@hdu.edu.cn).

Materials availability

All materials available on request from the authors.

Data and code availability

Data available on request from the authors.

Fabrication of self-powered sensor

A piece of copper film with a size of 1.6 × 1.0 × 0.01 cm was cut from the copper foil tape. Then the copper film bonds together with a PTFE film that possesses dimensions of 1.6 × 1.0 × 0.03 cm. The PTFE film was rinsed with alcohol/isopropyl alcohol and deionized water, then blow-dried with nitrogen, and inductively coupled plasma (ICP, SI500, SENTECH Instruments Corp.) was adopted to etch the PTFE film. The Cu foil attached to the PTFE film will be the one electrode. A metal sputtering technique was adopted to deposit a coating of Al on the Kapton substrate to compose another flexible conductive electrode. We select the hydrophobic materials (PTFE and Porous Al) as the two triboelectric layers to refrain the humidity interference from the water film or molecules. The contact angles of two triboelectric layers are 110.7 and 93.7°, respectively (Figure S11).

Fabrication of the RMS

Briefly, two polymethyl methacrylate (PMMA) films that were laser-cut into a specified shape, stuck tightly on each side of PDMS foil with inner dimensions of 1.6 × 1.0 × 0.05 cm, was designed to create the main structure for the proposed sensor patch. PDMS was used as an elastic substrate to improve the stability of the system and the comfort for users; it has eco-friendliness as well. The PTFE-Cu layer is adhered to the PDMS substrate by the pressure sensitive adhesive. First, an aluminum film was sputtered on the bottom surface of a Kapton membrane to form a new layer renamed the Kapton-Al layer. The aluminum film was not only the friction layer, but also one of the electrodes of the TENG. Meanwhile, the PDMS basilar membrane was cut into a rectangle as well, as the copper pipe was used as a part of the electrode which was fitted with a flexible cylindrical structure for fixing the movable membrane. Finally, another Cu film was attached to the PDMS substrate as an electrode and the PTFE film applied to the upper surface of copper. The device has an extremely small weight of 0.402 g. As illustrated in Figure S5, two lead wires were connected to the two electrodes by copper foil tape.

Characterization

The short-circuit current and open-circuit voltage were measured using a Keithley electrometer system (Keithley 6514). A commercial humidifier (TaoTronics Ultrasonic Humidifiers) was used to increase the humidity in the environment in which the sensor was located. For testing the performance of the sensor, a temperature controller (GYTC100) was adopted. The electrical shielding box covered by aluminum film was used to shield the ambient noise during the output electrical performance test. The self-powered respiration sensor was attached to the volunteer's skin below the nose, the human respiration behaviors lead to the electric outputs of the device. The output electrical performance was measured to estimate the performance of the device. Simultaneously, the host computer platform was constructed on the basis of Qt Creator software to realize the processing, alarm, and display of the signal.

Experimental setup

In this study, as the voltage signal is first transmitted to the main control module and finally to the mobile phone terminal wirelessly, it is crucial for the system to match the relevant parameters between the signal and the control module. The hardware module, which consists of a voltage follower, a voltage lifting circuit, a main control chip, and a wireless transmission module, was integrated into a circuit board. In this paper, Multisim is used for preliminary design and simulation of the circuit board. Then, Altium Designer software for the final layout design and wiring

of the circuit board to accomplish the acquiring, processing, and wireless transmitting of the corresponding voltage signal. Last, we developed the human-computer interaction system on account of the Android system. In detail, the LM358 operational amplifier chip and the surrounding resistance and capacitance circuit are used to achieve the impedance matching of the system. The output AC voltage of the RMS does not conform to the signal input amplitude range of the ADC part in a micro control unit (MCU), the TLC074 module circuit is adapted to achieve the voltage regulation and the system filter function related with the power supply module. Wireless data transmission relies on a tiny Bluetooth module, and the cloud platform is used for remote data collection and processing. This study was approved by the local research ethics committee (No. 2021-IRB-041). Informed consent was obtained from human participants of this study and all related experiments were completed in 2021 in the period of validity of the local research ethics committee.

SUPPLEMENTAL INFORMATION

Supplemental information can be found online at https://doi.org/10.1016/j.xcrp.2022.101191.

ACKNOWLEDGMENTS

This work was financially supported by the National Natural Science Foundation of China (no. 62111530298, U1909221, 61871167) and the Key Research and Development Plan Project of Zhejiang Province (no. 2018C01036).

AUTHOR CONTRIBUTIONS

Y.L. and C.L. performed the experiment and analyzed the data. H.Z. and L.C. fabricated the RMS and accomplished characterization. P.S., J.Y., W.L., X.W., and Z.X. provided valuable advice in the RMS system. W.Y., L.D., L.Z., G.W., and Z.L.W. initialized the idea, designed the experiment, and analyzed the data.

DECLARATION OF INTERESTS

The authors declare no competing interests.

Received: August 15, 2022
Revised: September 30, 2022
Accepted: November 22, 2022
Published: January 3, 2023

REFERENCES

1. Vasandani, P., Gattu, B., Wu, J., Mao, Z.-H., Jia, W., and Sun, M. (2017). Triboelectric nanogenerator using microdome-patterned PDMS as a wearable respiratory energy harvester. Adv. Mater. Technol. *2*. 1700014. https://doi.org/10.1002/admt.201700014.

2. Wang, S., Jiang, Y., Tai, H., Liu, B., Duan, Z., Yuan, Z., Pan, H., Xie, G., Du, X., and Su, Y. (2019). An integrated flexible self-powered wearable respiration sensor. Nano Energy *63*. 103829. https://doi.org/10.1016/j.nanoen.2019.06.025.

3. Shu, S., An, J., Chen, P., Liu, D., Wang, Z., Li, C., Zhang, S., Liu, Y., Luo, J., and Zu, L. (2021). Active-sensing epidermal stretchable bioelectronic patch for Noninvasive,Conformal,and wireless tendon monitoring. Research *12*. 9783432.

4. Peng, X., Dong, K., Ning, C., Cheng, R., Yi, J., Zhang, Y., Sheng, F., Wu, Z., and Wang, Z.L. (2021). All-nanofiber self-powered skin-interfaced real-time respiratory monitoring system for obstructive sleep apnea-hypopnea syndrome diagnosing. Adv. Funct. Mater. *31*. 2103559. https://doi.org/10.1002/adfm.202103559.

5. Bai, Z., He, T., Zhang, Z., Xu, Y., Zhang, Z., Shi, Q., Yang, Y., Zhou, B., Zhu, M., Guo, J., and Lee, C. (2022). Constructing highly tribopositive elastic yarn through interfacial design and assembly for efficient energy harvesting and human-interactive sensing. Nano Energy *94*. 106956. https://doi.org/10.1016/j.nanoen.2022.106956.

6. Xue, H., Yang, Q., Wang, D., Luo, W., Wang, W., Lin, M., Liang, D., and Luo, Q. (2017). A wearable pyroelectric nanogenerator and self-powered breathing sensor. Nano Energy *38*, 147–154. https://doi.org/10.1016/j.nanoen.2017.05.056.

7. Jiang, Q., Chen, B., Zhang, K., and Yang, Y. (2017). Ag nanoparticle-based triboelectric nanogenerator to scavenge wind energy for a self-charging power unit. ACS Appl. Mater. Interfaces *9*, 43716–43723. https://doi.org/10.1021/acsami.7b14618.

8. Zhao, X., Chen, B., Wei, G., Wu, J.M., Han, W., and Yang, Y. (2019). Polyimide/graphene

nanocomposite foam-based wind-driven triboelectric nanogenerator for self-powered pressure sensor. Adv. Mater. Technol. *4*. 1800723. https://doi.org/10.1002/admt.201800723.

9. Zhang, Z., Zhang, J., Zhang, H., Wang, H., Hu, Z., Xuan, W., Dong, S., and Luo, J. (2019). A portable triboelectric nanogenerator for real-time respiration monitoring. Nanoscale Res. Lett. *14*, 354. https://doi.org/10.1186/s11671-019-3187-4.

10. Park, S.W., Das, P.S., Chhetry, A., and Park, J.Y. (2017). A flexible capacitive pressure sensor for wearable respiration monitoring system. IEEE Sens. J. *17*, 6558–6564. https://doi.org/10.1109/jsen.2017.2749233.

11. Zhao, X., Zhang, D., Xu, S., Qian, W., Han, W., Wang, Z.L., and Yang, Y. (2020). Stretching-enhanced triboelectric nanogenerator for efficient wind energy scavenging and ultrasensitive strain sensing. Nano Energy *75*. 104920. https://doi.org/10.1016/j.nanoen.2020.104920.

12. Chen, X., Ma, X., Ren, W., Gao, L., Lu, S., Tong, D., Wang, F., Chen, Y., Huang, Y., He, H., et al. (2020). A triboelectric nanogenerator exploiting the Bernoulli effect for scavenging wind energy. Cell Rep. Phys. Sci. *1*. 100207. https://doi.org/10.1016/j.xcrp.2020.100207.

13. Jiang, Q., Chen, B., and Yang, Y. (2018). Wind-driven triboelectric nanogenerators for scavenging biomechanical energy. ACS Appl. Energy Mater. *1*, 4269–4276. https://doi.org/10.1021/acsaem.8b00902.

14. Sun, Z., Zhu, M., Zhang, Z., Chen, Z., Shi, Q., Shan, X., Yeow, R.C.H., and Lee, C. (2021). Artificial intelligence of things (AIoT) enabled virtual shop applications using self-powered sensor enhanced soft robotic manipulator. Adv. Sci. *8*. e2100230. https://doi.org/10.1002/advs.202100230.

15. Wen, F., Zhang, Z., He, T., and Lee, C. (2021). AI enabled sign language recognition and VR space bidirectional communication using triboelectric smart glove. Nat. Commun. *12*, 5378. https://doi.org/10.1038/s41467-021-25637-w.

16. Luo, Y., Pei, Y., Feng, X., Zhang, H., Lu, B., and Wang, L. (2020). Silk fibroin based transparent and wearable humidity sensor for ultra-sensitive respiration monitoring. Mater. Lett. *260*. 126945. https://doi.org/10.1016/j.matlet.2019.126945.

17. Wang, M., Zhang, J., Tang, Y., Li, J., Zhang, B., Liang, E., Mao, Y., and Wang, X. (2018). Air-flow-driven triboelectric nanogenerators for self-powered real-time respiratory monitoring. ACS Nano *12*, 6156–6162. https://doi.org/10.1021/acsnano.8b02562.

18. Wang, S., Tai, H., Liu, B., Duan, Z., Yuan, Z., Pan, H., Su, Y., Xie, G., Du, X., and Jiang, Y. (2019). A facile respiration-driven triboelectric nanogenerator for multifunctional respiratory monitoring. Nano Energy *58*, 312–321. https://doi.org/10.1016/j.nanoen.2019.01.042.

19. Yang, Y., Shi, Q., Zhang, Z., Shan, X., Salam, B., and Lee, C. (2022). Robust triboelectric information-mat enhanced by multi-modality deep learning for smart home. InfoMat. e12360. https://doi.org/10.1002/inf2.12360.

20. Zhang, Z., Shi, Q., He, T., Guo, X., Dong, B., Lee, J., and Lee, C. (2021). Artificial intelligence of toilet (AI-Toilet) for an integrated health monitoring system (IHMS) using smart triboelectric pressure sensors and image sensor. Nano Energy *90*. 106517. https://doi.org/10.1016/j.nanoen.2021.106517.

21. Fan, F.R., Tian, Z.Q., and Lin Wang, Z. (2012). Flexible triboelectric generator. Nano Energy *1*, 328–334.

22. Zhu, G., Lin, Z.H., Jing, Q., Bai, P., Pan, C., Yang, Y., Zhou, Y., and Wang, Z.L. (2013). Toward large-scale energy harvesting by a nanoparticle-enhanced triboelectric nanogenerator. Nano Lett. *13*, 847–853.

23. Mhetre, M.R., and Abhyankar, H.K. (2017). Human exhaled air energy harvesting with specific reference to PVDF film. Eng. Sci. Technol. Int. J. *20*, 332–339.

24. Zhou, Y.S., Liu, Y., Zhu, G., Lin, Z.H., Pan, C., Jing, Q., and Wang, Z.L. (2013). In situ quantitative study of nanoscale triboelectrification and patterning. Nano Lett. *13*, 2771–2776.

25. Zou, H., Guo, L., Xue, H., Zhang, Y., Shen, X., Liu, X., Wang, P., He, X., Dai, G., Jiang, P., et al. (2020). Quantifying and understanding the triboelectric series of inorganic non-metallic materials. Nat. Commun. *11*, 2093.

26. Zou, H., Dai, G., Wang, A.C, Li, X., and Wang, Z.L. (2020). Alternating Current Photovoltaic Effect. Adv. Mater. *32* (21). https://doi.org/10.1002/adma.202001532.

27. Liu, C., Fang, L., Zou, H., Wang, Y., Chi, J., Che, L., Zhou, X., Wang, Z., Wang, T., Dong, L., et al. (2021). Theoretical investigation and experimental verification of the self-powered acceleration sensor based on triboelectric nanogenerators (TENGs). Extreme Mech. Lett. *42*. 101021.

28. Liu, C., Wang, Y., Zhang, N., Yang, X., Wang, Z., Zhao, L., Yang, W., Dong, L., Che, L., Wang, G., and Zhou, X. (2020). A self-powered and high sensitivity acceleration sensor with V-Q-a model based on triboelectric nanogenerators (TENGs). Nano Energy *67*. 104228.

29. Sun, W., Ding, Z., Qin, Z., Chu, F., and Han, Q. (2020). Wind energy harvesting based on fluttering double-flag type triboelectric nanogenerators. Nano Energy *70*. 104526. https://doi.org/10.1016/j.nanoen.2020.104526.

30. Olsen, M., Zhang, R., Örtegren, J., Andersson, H., Yang, Y., and Olin, H. (2019). Frequency and voltage response of a wind-driven fluttering triboelectric nanogenerator. Sci. Rep. *9*, 5543. https://doi.org/10.1038/s41598-019-42128-7.

31. Wang, Y., Yang, E., Chen, T., Wang, J., Hu, Z., Mi, J., Pan, X., and Xu, M. (2020). A novel humidity resisting and wind direction adapting flag-type triboelectric nanogenerator for wind energy harvesting and speed sensing. Nano Energy *78*. 105279. https://doi.org/10.1016/j.nanoen.2020.105279.

32. Xu, Q., Lu, Y., Zhao, S., Hu, N., Jiang, Y., Li, H., Wang, Y., Gao, H., Li, Y., Yuan, M., et al. (2021). A wind vector detecting system based on triboelectric and photoelectric sensors for simultaneously monitoring wind speed and direction. Nano Energy *89*. 106382. https://doi.org/10.1016/j.nanoen.2021.106382.

33. Undi, T., Marco, S., Perera, A., Pardo, A., Hahn, S., Bârsan, N., and Weimar, U. (2002). Fuzzy inference system for sensor array calibration: prediction of CO and CH 4 levels in variable humidity conditions. Chemometr. Intell. Lab. Syst. *64*, 103–122.

34. Liu, L., Fei, T., Guan, X., Zhao, H., and Zhang, T. (2021). Humidity-activated ammonia sensor with excellent selectivity for exhaled breath analysis. Sensor. Actuator. B Chem. *334*. 129625. https://doi.org/10.1016/j.snb.2021.129625.

35. Tabyshova, A., Hurst, J.R., Soriano, J.B., Checkley, W., and Boven, J. (2020). Gaps in COPD guidelines of low- and middle-income countries: a systematic scoping review. Chest *159*, 575–584.

36. Bangash, M.N., Owen, A., Alderman, J.E., Chotalia, M., Patel, J.M., and Parekh, D. (2020). COVID-19 recovery: potential treatments for post-intensive care syndrome. Lancet Respir. Med. *8*, 1071–1073. https://doi.org/10.1016/s2213-2600(20)30457-4.

37. Stull, D.E., Schaefer, M., Crespi, S., and Sandor, D.W. (2009). Relative strength of relationships of nasal congestion and ocular symptoms with sleep, mood and productivity. Curr. Med. Res. Opin. *25*, 1785–1792.

38. Lunn, M., and Craig, T. (2011). Rhinitis and sleep. Sleep Med. Rev. *15*, 293–299. https://doi.org/10.1016/j.smrv.2010.12.001.

39. Tonkin, J., and Leaver, S.K. (2018). Sleep disorders. Medicine *46*, 767–773. https://doi.org/10.1016/j.mpmed.2018.09.008.

40. Zhang, J., Yang, X.C., Luo, L., Shao, J., Zhang, C., Ma, J., Wang, G.F., Liu, Y., Peng, C.K., and Fang, J. (2009). Assessing severity of obstructive sleep apnea by fractal dimension sequence analysis of sleep EEG. Phys. Stat. Mech. Appl. *388*, 4407–4414. https://doi.org/10.1016/j.physa.2009.07.005.

41. Kurniyanto, Setianegari, Y., Kurniaty, L., Luhulima, D.E.J., Utomo, B.S.R., Langi, L.A., Ronny, Arodes, E.S., Arodes, E.S., Wiyanto, M., Suarthana, E., and Wahyuningsih, R. (2022). Factors associated with death and ICU referral among COVID-19 patients hospitalized in the secondary referral academic hospital in East Jakarta, Indonesia. J. Clin. Virol. *2*. 100068. https://doi.org/10.1016/j.jcvp.2022.100068.

42. Kamran, S.M., Mirza, Z.E.H., Moeed, H.A., Naseem, A., Hussain, M., Fazal, I., Saeed, F., Alamgir, W., Saleem, S., Riaz, S., and Riaz, S. (2020). CALL score and RAS score as predictive models for coronavirus disease 2019. Cureus *12*. e11368. https://doi.org/10.7759/cureus.11368.

43. Grasselli, G., Tonetti, T., Protti, A., Langer, T., Girardis, M., Bellani, G., Laffey, J., Carrafiello, G., Carsana, L., Rizzuto, C., et al. (2020). Pathophysiology of COVID-19-associated acute respiratory distress syndrome: a multicentre prospective observational study. Lancet Respir. Med. *8*,

1201–1208. https://doi.org/10.1016/s2213-2600(20)30370-2.

44. Al Armashi, A.R., Somoza-Cano, F.J., Patell, K., Homeida, M., Desai, O., Zubaidi, A.A., Altaqi, B., and Ravakhah, K. (2021). Spontaneous pneumomediastinum: a collaborative sequelae between COVID-19 and self-inflicted lung injury - a case report and literature review. Radiol. Case Rep. *16*, 3655–3658. https://doi.org/10.1016/j.radcr.2021.08.076.

45. Zhu, M., Sun, Z., Chen, T., and Lee, C. (2021). Low cost exoskeleton manipulator using bidirectional triboelectric sensors enhanced multiple degree of freedom sensory system. Nat. Commun. *12*, 2692. https://doi.org/10.1038/s41467-021-23020-3.

46. Kr, A., Vsma, B., Bkp, A., Sg, A., and Mg, A. (2021). Asymptomatic infection and transmission of COVID-19 among clusters: systematic Review and Meta-Analysis. Publ. Health *203*, 100–109. ScienceDirect.